



Assessing the impact of ENSO on drought in the U.S. Southwest with NCEP climate model simulations



Hui Wang^{a,b,*}, Arun Kumar^a

^aNOAA/NWS/NCEP/Climate Prediction Center, College Park, MD, USA

^bInnovim, Greenbelt, MD, USA

ARTICLE INFO

Article history:

Available online 20 December 2014

Keywords:

Drought
U.S. Southwest
El Niño–Southern Oscillation (ENSO)
Climate model simulation

SUMMARY

The impact of El Niño–Southern Oscillation (ENSO) on U.S. Southwest precipitation and drought is assessed based on observational data and coupled global climate model simulations. The co-variability between 67-year (1948–2014) Southwest winter precipitation and Pacific sea surface temperature (SST) is analyzed using the singular value decomposition method. Results indicate strong associations between Southwest drought and La Niña during 1948–1977 and between Southwest pluvial and El Niño during 1978–1999. The relationship between Southwest precipitation and tropical Pacific SST is relatively weak after 1999. A comparison between two 480-year model simulations with and without ENSO variability suggests that ENSO can alter the characteristics of precipitation, and thus droughts over the Southwest in terms of frequency and intensity. In the presence of ENSO, the variability of Southwest precipitation is enhanced, and further, shifts toward lower frequencies. In addition, the chance for the ENSO-related precipitation pattern to persist over 3–4 years in the Southwest is higher in the simulation with ENSO than that without ENSO. The modeling study also demonstrates a sensitivity of the Southwest precipitation-related teleconnection to both the phase and intensity of ENSO, which helps understand the observed decadal changes in the strength of the link between Southwest precipitation and ENSO.

© 2014 Elsevier B.V. All rights reserved.

1. Introduction

A severe drought has been afflicting the U.S. Southwest for the past several years. California, the most populated state in the country, is now facing one of the worst droughts on record (Funk et al., 2014; Swain et al., 2014; Wang et al., 2014). Although La Niña has been recognized as the major driver of precipitation deficits and droughts in the U.S. Southwest (e.g., Seager et al., 2008; Mo et al., 2009; Cook et al., 2011), it might not be the contributing factor to the present drought because an El Niño–Southern Oscillation (ENSO) neutral condition has been in place since the termination of 2010/11 La Niña and there is a moderate El Niño underway.

Precipitation and droughts over the U.S. Southwest exhibit variations on both interannual and decadal timescales. Their interannual variability is closely related to ENSO in the tropical Pacific (Ropelewski and Halpert, 1986; Andrade and Sellers, 1988; Wang and Ting, 2000; Schubert et al., 2009), whereas the decadal variability is associated with various climate variations in both the

atmosphere and oceans (e.g., Cayan et al., 1998; Dettinger et al., 1998; McCabe et al., 2004; Cook et al., 2011). The strength of the linkage between ENSO and precipitation over the Southwest, which is on the interannual timescale, has also displayed decadal variations (McCabe and Dettinger, 1999), subject to the phase of the Pacific Decadal Oscillation (PDO; Mantua et al., 1997).

ENSO, the major source of global and regional climate variability on the interannual timescale, has also experienced significant decadal changes in terms of intensity and occurrence (Wang, 1995; Trenberth and Hoar, 1996; Trenberth and Stepaniak, 2001; Tang et al., 2008; Hu et al., 2013; Ogata et al., 2013). Given the strong association between ENSO and precipitation over the Southwest, it is expected that the decadal changes in ENSO may also affect the precipitation variability over the Southwest on the decadal timescale, and thus provide a source of the decadal variability of precipitation over this region.

The present study is aimed at investigating how the decadal variations of ENSO, via its linkage with precipitation, modulate drought over the U.S. Southwest. The impact of ENSO on Southwest precipitation and drought is assessed through the analysis and comparison of global climate model simulations with and without ENSO variability. Two 500-year simulations were conducted. The first one is a fully coupled run that retains the ENSO variability

* Corresponding author at: NOAA Climate Prediction Center, 5830 University Research Court, NCWCP, College Park, MD 20740, USA. Tel.: +1 301 683 3397.

E-mail addresses: hui.wang@noaa.gov (H. Wang), arun.kumar@noaa.gov (A. Kumar).

(referred to as ENSO run hereafter). In the second run, model predicted daily sea surface temperature (SST) in the tropical Pacific is relaxed to follow the climatological seasonal cycle of daily SST derived from observations. In this way, the variability in tropical Pacific SST, which is dominated by ENSO, is removed from the 500-yr model integration (referred to as no-ENSO run hereafter). The differences in the characteristics of U.S. Southwest precipitation between the ENSO run and no-ENSO run are interpreted as the influence of ENSO.

Among the questions we will address are: what is the relationship between ENSO and precipitation over the U.S. Southwest? Are the characteristics of Southwest precipitation, such as intensity and frequency, modulated by ENSO? Is the relationship between Southwest precipitation and ENSO sensitive to the phase and intensity of ENSO? How do the decadal variations of ENSO affect the variability of droughts over the Southwest?

This paper is organized as follows. Section 2 provides a brief description of the data, model experiment design and methodology used. The characteristics of long-term mean and variability of U.S. winter precipitation, the ENSO-related Southwest drought and precipitation in observations and simulations, and the changes in the statistics of Southwest precipitation due to ENSO, as well as the sensitivity of atmospheric circulation response to ENSO are examined in Section 3. Conclusions are given in Section 4.

2. Data and model experiments

Our analysis is based on the data derived from both observations and simulations with a coupled model. The observational data consist of precipitation, SST, sea level pressure (SLP), 850-hPa and 200-hPa winds, and 200-hPa geopotential height. The precipitation data are taken from the National Oceanic and Atmospheric Administration (NOAA) Precipitation Reconstruction over Land (PREC/L) dataset (Chen et al., 2002) on a $1^\circ \times 1^\circ$ (latitude \times longitude) grid. The SSTs are the NOAA Extended Reconstructed SST (ERSST) version 3b (Smith et al., 2008) with a $2^\circ \times 2^\circ$ resolution. The SLP, atmospheric winds, and height field are from the National Centers for Environmental Prediction–National Center for Atmospheric Research (NCEP–NCAR) Reanalysis product (Kalnay et al., 1996) on a $2.5^\circ \times 2.5^\circ$ grid. All the observational data cover a 67-year period from 1948 to 2014.

The model data are from the simulations with the NCEP Climate Forecast System (CFS) coupled model (Saha et al., 2006). The atmospheric, oceanic, and land components of the CFS are the NCEP Global Forecast System (GFS) version 1 (Moorthi et al., 2001), the Geophysical Fluid Dynamics Laboratory (GFDL) Modular Ocean Model version 3 (MOM3; Pacanowski and Griffies, 1998), and the Oregon State University (OSU) land surface model (LSM; Pan and Mahrt, 1987), respectively.

In this version of the CFS, the atmospheric GFS has a horizontal resolution of T62 and 64 vertical levels. The GFDL MOM3 covers global oceans from 74°S to 64°N , with horizontal resolutions of 1° (longitude) by $1/3^\circ$ (latitude) between 10°S and 10°N , and increasing to 1° (latitude) poleward of 30°S and 30°N . The ocean model has 40 layers from 5 m below sea level to 4479 m, with a 10-m resolution in the upper 240 m. The OSU LSM has two soil layers, 0–10 cm and 10–190 cm. More detailed descriptions of the CFS can be found in Saha et al. (2006).

The coupled model was integrated over 500 years for both the ENSO run and no-ENSO run. The ENSO run is a coupled simulation which allows full air–sea interaction over the global oceans and simulates ENSO variability. In the no-ENSO run, the ENSO SST variability is removed by assimilating the daily SST climatology into the CFS in the tropical Pacific domain (140°E – 75°W , 10°S – 10°N). This was done by replacing the model predicted SST in this region

with a new SST (SST_{new}) after one day of coupled model integration. The new SST is a combination of the model SST predicted by the MOM3 (SST_{MOM3}) and observed daily SST climatology (SST_{OBS}) based on the following:

$$\text{SST}_{\text{new}} = (1 - w) \times \text{SST}_{\text{MOM3}} + w \times \text{SST}_{\text{OBS}},$$

where w is a weighting coefficient, and is set to $1/3$ in the tropical Pacific domain (140°E – 75°W , 10°S – 10°N) and is linearly reduced to 0 on the border of an extended domain (130°E – 65°W , 15°S – 15°N). The observed daily SST climatology was interpolated from the long-term mean monthly SST derived from the NOAA Optimum Interpolation SST (OISST) V2 (Reynolds et al., 2002) over the 1981–2008 period. The use of SST_{OBS} with $w = 1/3$ is equivalent to relaxing the model-produced SST to the observed climatology with an e-folding time of 3.3 days, which effectively removes the inter-annual variability of SST in the tropical Pacific, including El Niño and La Niña. This set of two 500-year simulations has been used to examine the ENSO variability (Kim et al., 2012), the PDO (Wang et al., 2012a; Kumar et al., 2013), and the impact of ENSO on the PDO (Wang et al., 2012b).

For both the ENSO run and no-ENSO run, the last 480 years of the simulations are used in this study. The analysis focuses on boreal winter because the impact of ENSO on the northern extratropics is strongest during this season and also winter precipitation contributes to the greatest percentage of annual rainfall in the U.S. Southwest (not shown). As illustrated in Wang and Fu (2000), the typical ENSO-induced U.S. winter precipitation pattern emerges in January and continues through March. Therefore, data averaged over January, February, and March (JFM) is used as the winter seasonal mean.

The singular value decomposition (SVD; Bretherton et al., 1992) is employed to objectively identify a pair of spatial patterns of U.S. precipitation and Pacific SST in observations with maximum temporal covariance between the two fields (e.g., Ting and Wang, 1997; Wang and Ting, 2000). Correlation and linear regression against same precipitation based time series are used to document the drought-related atmospheric teleconnection, as well as the associated circulation anomalies. The statistical significance of the correlation coefficients is estimated by the two-tailed t-test.

3. Results

3.1. Long-term mean and variability of U.S. winter precipitation

The long-term average U.S. winter precipitation shown in Fig. 1a is characterized by abundant rainfall ($> 4 \text{ mm day}^{-1}$) in the Pacific Northwest coastal region, northern California, and the Gulf States. The precipitation maximum in the Pacific Northwest is associated with frequent North Pacific winter storms, while large mean precipitation in the Southeast is due to ample moisture supply from the Gulf of Mexico. The Great Plains are dry in winter with mean precipitation less than 1 mm day^{-1} .

The climatology of winter precipitation in both the ENSO run (Fig. 1b) and no-ENSO run (Fig. 1c) displays a spatial pattern similar to the observations. However, the model simulated mean precipitation is greater than the observed across the U.S. as a whole. The bias is partially due to the low resolution of the model. A recent study (Jia et al., 2015) indicates that a high-resolution global climate model can obtain better precipitation climatology than a low-resolution model. It is noted that there are no significant differences in the mean precipitation between the ENSO run and no-ENSO run, with the largest differences (0.5 – 0.9 mm day^{-1}) in California and Florida and relatively small differences ($< 0.5 \text{ mm day}^{-1}$) in the rest of the country (not shown).

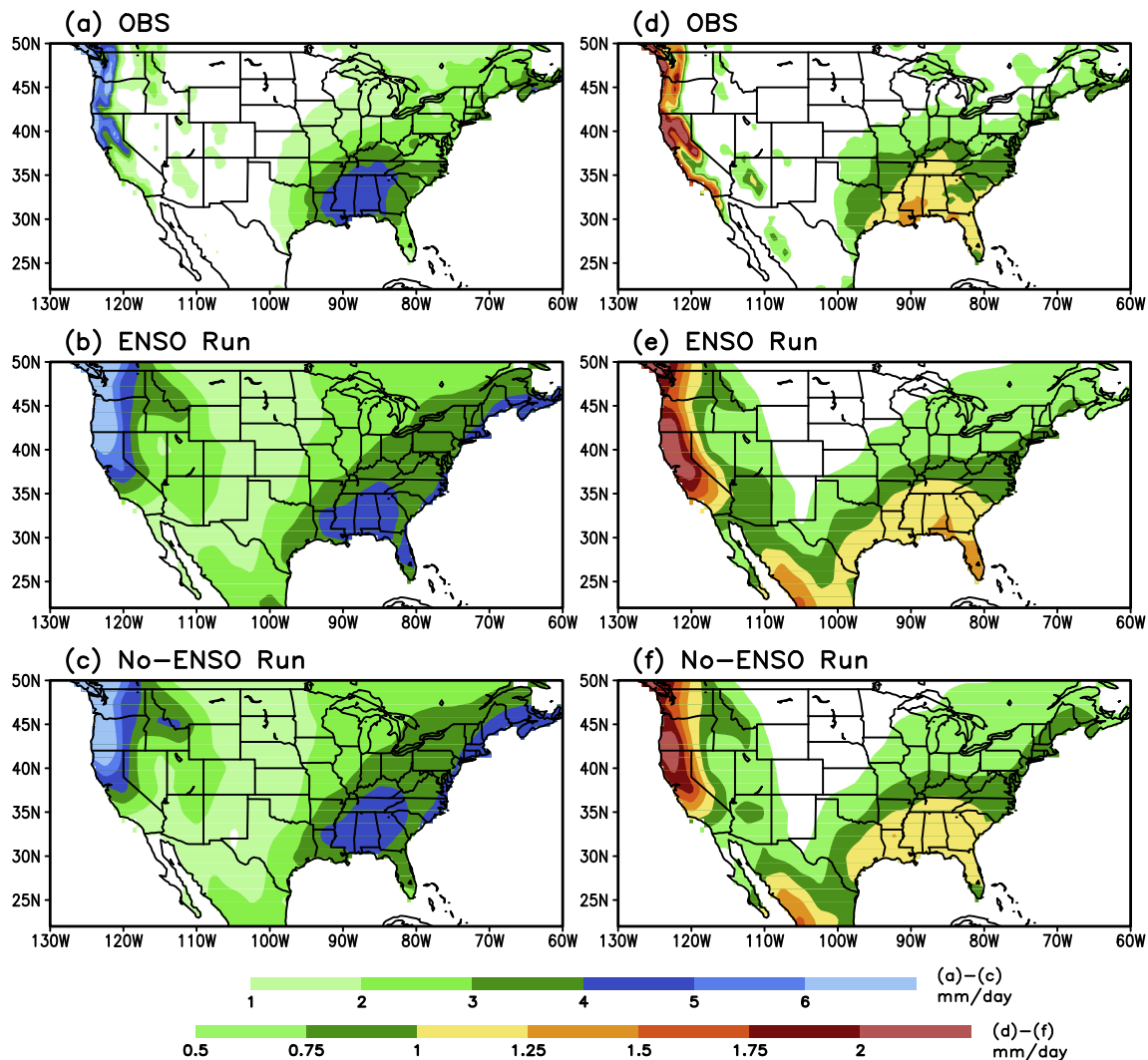


Fig. 1. Long-term average winter (JFM) seasonal mean (left) and standard deviation (right) of precipitation for (a), (d) observations (1948–2014) and 480-year (b), (e) ENSO run and (c), (f) no-ENSO run. The upper color bar is for left panels and the lower color bar for right panels, both with the unit of mm day^{-1} . (For interpretation of the references to color in this figure legend, the reader is referred to the web version of this article.)

The variability of winter precipitation, which is quantified by the standard deviation of JFM mean precipitation, is also shown in Fig. 1 (right panels). In both the observations and model simulations, regions of large mean precipitation are usually accompanied by large precipitation variability. Over most of the U.S., the variability of winter precipitation in the no-ENSO run is comparable to that in the ENSO run, except California and Florida where standard deviation of precipitation in the no-ENSO run is slightly less than in the ENSO run.

A visual assessment of Fig. 1 suggests that the observed spatial patterns of both the mean and variability of U.S. winter precipitation are simulated reasonably well in the CFS. The overall resemblance of the precipitation statistics between the observations and simulations gives us confidence in assessing the possible influence of ENSO on U.S. winter precipitation through a comparison between the ENSO run and no-ENSO run.

3.2. ENSO-related drought in observations

To quantify the association between drought in the U.S. Southwest and La Niña in the tropical Pacific, an SVD analysis is performed by analyzing the covariance matrices of winter season U.S. precipitation and Pacific SST with observational data. The

spatial patterns of the first SVD mode are shown in Fig. 2a for precipitation and Fig. 2b for SST, as the maps of homogeneous correlation (Wallace et al., 1992) and regression coefficient against the corresponding SVD time series shown in Fig. 2c.

The first SVD mode of precipitation (Fig. 2a), which explains 19% of the total U.S. winter precipitation variance, has a well-defined pattern over the Southwest with large negative correlations. Negative correlations are also found in the central and southern plains and in the regions along the southeast coast. Positive correlations are found in the areas extending from the Ohio River valley to the Great Lakes. This is the typical winter precipitation pattern related to the cold phase of ENSO identified and documented in many previous studies (e.g., Ropelewski and Halpert, 1986; Wang and Ting, 2000). Associated with a one-standard-deviation departure in the SVD precipitation time series, below-normal precipitation anomalies in California exceed -1 mm day^{-1} . We also note that the first SVD mode of precipitation is almost identical to the leading empirical orthogonal function (EOF) of the observed U.S. winter precipitation, with a pattern correlation of 0.97 between the SVD (Fig. 2a) and EOF (not shown) patterns of precipitation and a temporal correlation of 0.95 between the SVD (Fig. 2c) and EOF (not shown) time series.

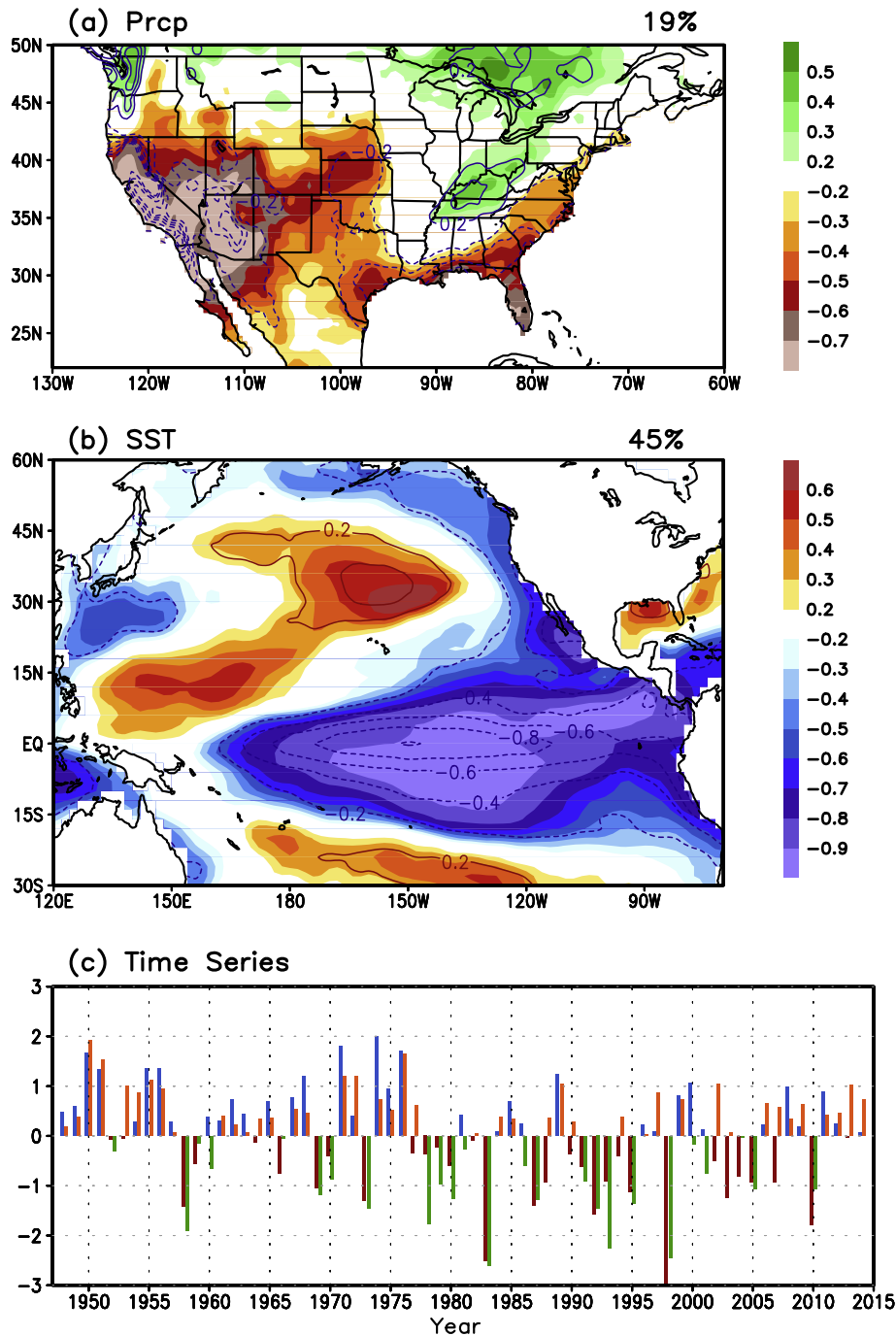


Fig. 2. Homogeneous correlation (shadings) and regression coefficient (contours) of the first SVD mode between winter (a) U.S. precipitation and (b) Pacific SST, and (c) corresponding normalized SVD time series for precipitation (green and orange bars) and SST (red and blue bars) based on observational data from 1948 to 2014. The percentage of the variance explained by this mode is given at the top right of (a) and (b) for the precipitation and SST fields, respectively. The regression coefficient is equivalent to precipitation and SST anomalies associated one-standard-deviation departure in their corresponding SVD time series. The contour interval is 0.2 mm day⁻¹ in (a) and 0.2 K in (b) with negative contours dashed and zero contours omitted. (For interpretation of the references to color in this figure legend, the reader is referred to the web version of this article.)

The SST component of the first SVD mode explains 45% of the total SST variance. The spatial pattern (Fig. 2b) is characterized by the canonical La Niña SST distribution, with large negative correlations in the eastern and central tropical Pacific, which interpose themselves between positive correlations in the northern and southern subtropical Pacific. Additional positive correlations are located in the central North Pacific and negative correlations along the coast of North America. Associated with a one-standard-deviation departure in the SVD SST time series, La Niña SST anomalies can be below -1 K near 150° W at the equator.

The temporal correlation between the precipitation and SST time series of the first SVD mode (Fig. 2c) is 0.77, above the 99% two-tailed significance level. The SST time series displays large positive (blue bars) and negative (red bars) fluctuations (exceeding \pm one standard deviation) in La Niña (1950, 1951, 1955, 1956, 1968, 1971, 1974, 1976, 1989, 2000, and 2008) and El Niño (1958, 1969, 1973, 1983, 1987, 1992, 1995, 1998, 2003, and 2010) years, respectively. Consistently, the precipitation time series also exhibits large positive (orange bars) and negative (green bars) departures from the mean during La Niña (El Niño) years.

This indicates a close relationship between dry (wet) conditions in the U.S. Southwest and cold (warm) phase of ENSO SST in the tropical Pacific on the interannual timescale. The first SVD mode accounts for 85% of the covariance between the SST and precipitation fields, suggesting a dominant role of ENSO in the co-variability between winter U.S. precipitation and Pacific SST.

It is also evident that the first SVD mode captures decadal variations in both precipitation and SST fields over the 67 years (Fig. 2c). In the first 30 years (1948–1977), both the SST and precipitation time series are dominated by positive values, with more La Niña events than El Niño (8 vs. 3). Consequently, precipitation deficits and the associated droughts prevailed over the U.S. Southwest in the early years, especially in the 1950s. During the 1978–1999 period, El Niño became more frequent than La Niña (5 vs. 1), with the two strongest El Niño events occurring in 1982/83 and 1997/98 winters. These warm ENSO events brought significant storms and extreme precipitation across the Southwest, causing floods and mud slides in California. In the most recent period (2000–2014), the variations of SST and precipitation are less coherent. The correlation between the two time series is 0.30 in the last 15 years (2000–2014). In contrast, the correlation is 0.84 in both the first 30 years (1948–1977) and the following 22 years (1978–1999). The association between U.S. Southwest precipitation and tropical Pacific SST in the early 21st century is not as strong as that in the second half of the 20th century. The timing of the changes in the co-variation between Southwest precipitation and SST coincided with the decadal change in ENSO phase in the late 1970s (Wang, 1995; Trenberth and Stepaniak, 2001) and the weakening of ENSO variability since 2000 (Hu et al., 2013).

3.3. ENSO-related drought in simulations

The variability of the precipitation pattern similar to the ENSO-related one found in the observations (Fig. 2a) is assessed for both the ENSO run and no-ENSO run. This was done by first projecting the model winter precipitation anomalies onto the observed precipitation pattern (Fig. 2a) to obtain a projection coefficient for each winter. Then, the variability of the 480-year time series of the projection coefficients was examined. The actual precipitation pattern in the simulations associated with the fluctuation of the projection coefficients can be reconstructed by the correlation or linear regression of the model precipitation anomalies with the time series of the projection coefficients. Fig. 3a and b show such a precipitation pattern for the ENSO run and no-ENSO run, respectively.

Using the above procedure, the reconstructed precipitation patterns in both simulations (Fig. 3) resemble the observed SVD1 precipitation distribution (Fig. 2a), with negative correlations in the U.S. Southwest, Southern Plains, and Southeast, and positive correlations in the northwestern and northeastern corners. The correlation and regression anomalies in the ENSO run are larger over the western part of the Southwest than in the no-ENSO run (0.7 vs. 0.5 for correlation; 1.2 mm day^{-1} vs. 0.8 mm day^{-1} for regression anomaly). The precipitation patterns in both simulations (Fig. 3) also resemble the second EOF pattern of corresponding model U.S. winter precipitation (not shown). For model simulations, the first EOF has high loadings in the Pacific Northwest, where the winter precipitation has large variability (Fig. 1, right panels), thereby explaining more variance than the second EOF.

The temporal correlation between the EOF2 time series and the projection coefficient time series is 0.78 in the ENSO run and 0.72 in the no-ENSO run. The pattern correlation between EOF2 and that in Fig. 3 is 0.88 in the ENSO run and 0.86 in the no-ENSO run. All of these correlation coefficients are above the 99% significance level. Therefore, the observed precipitation pattern associated with ENSO (Fig. 2a) is closely related to one of the leading EOF modes of U.S.

winter precipitation in the model simulations, even without the ENSO variability as evidence by the analysis of the no-ENSO run.

Although the spatial patterns of precipitation in Fig. 3a and b look similar and indicate that ENSO SST variability merely modulates a mode of internal variability that can exist without ENSO, the associated frequency characteristics of precipitation, in the presence of ENSO, can be significantly different from those in the absence of ENSO. Fig. 4 shows the power spectra of the 480-year time series of the precipitation projection coefficients in both simulations, together with the power spectra of the Niño 3.4 SST index in the ENSO run. The latter is characterized by high power at the interannual timescale with a peak at 5 years, indicating the dominant period of ENSO in the model. Consistently, the peak of the power spectra of the precipitation in the ENSO run is close to the peak of the Niño 3.4 index. In contrast, similar precipitation pattern in the no-ENSO run displays minimum power at 5 years, but more power at higher frequency with two peaks at 3 and 4 years. The results suggest that the presence of ENSO shifts the U.S. Southwest precipitation toward lower frequencies.

The impact of ENSO on the characteristics of U.S. Southwest winter precipitation is further illustrated in Fig. 5, which shows the probability density function (PDF) of JFM mean total precipitation (Fig. 5a) and both the PDF and cumulative density function (CDF) of JFM precipitation anomalies (Fig. 5b and c) at all data grids over the Southwest domain (32°N – 42°N , 102°W – 124°W) for both the ENSO run and no-ENSO run. While the PDF describes the probability of having a specific amount of precipitation, for example, a precipitation anomaly of -0.5 mm day^{-1} , the CDF gives the probability that precipitation anomalies will be found to have a value less than or equal to -0.5 mm day^{-1} . Both the PDF and CDF are derived for annual JFM mean precipitation, as well as for 3- and 5-year JFM mean precipitation. The longer-time (3 and 5 years) averages are used to assess the impact of ENSO on prolonged drought and wetness.

A comparison between the ENSO run and no-ENSO run indicates that with the ENSO variability, the probability of greater than 2 mm day^{-1} precipitation increases whereas the probability of less than 2 mm day^{-1} precipitation decreases (Fig. 5a, solid lines). The impact is most noticeable for total precipitation ranging from 0.5 to 1.5 mm day^{-1} . The changes in the PDF due to ENSO are more robust for 3- and 5-year mean winter precipitation (dash and dot lines in Fig. 5a). Therefore, the chance of large and prolonged winter mean precipitation over the Southwest is higher with the ENSO variability than without the ENSO variability. The influence of ENSO on winter seasonal mean precipitation over the Southwest should be a manifestation of the strong and systematic responses of daily precipitation to ENSO (Cayan et al., 1999).

For Southwest winter precipitation anomalies (Fig. 5b, solid lines), the PDF shows a higher (lower) density in the no-ENSO run than in the ENSO run when the absolute value of anomalies is less (greater) than 0.5 mm day^{-1} . This is also true for 3- and 5-year mean anomalies (dash and dot lines). Therefore, ENSO leads to stronger precipitation variability over the Southwest. The result is consistent with the finding of Seager and Hoerling (2014) that ocean variability enhances the precipitation variability over this region. The CDF (Fig. 5c) also contrasts the differences between the two runs, with higher probability of negative precipitation anomalies (dryness) and lower probability of positive anomalies (wetness) in the ENSO run than in the no-ENSO run.

The persistence of the ENSO-like precipitation patterns (Fig. 3a and b) is assessed by looking at the probability distribution of the number of consecutive years in which the sign of the projection coefficient remains unchanged (e.g., Pegion and Kumar, 2010), as shown in Fig. 5d. The probability of year-to-year switch of the sign of precipitation pattern is higher in the no-ENSO run than in the ENSO run. However, the chances of biennial precipitation anomaly

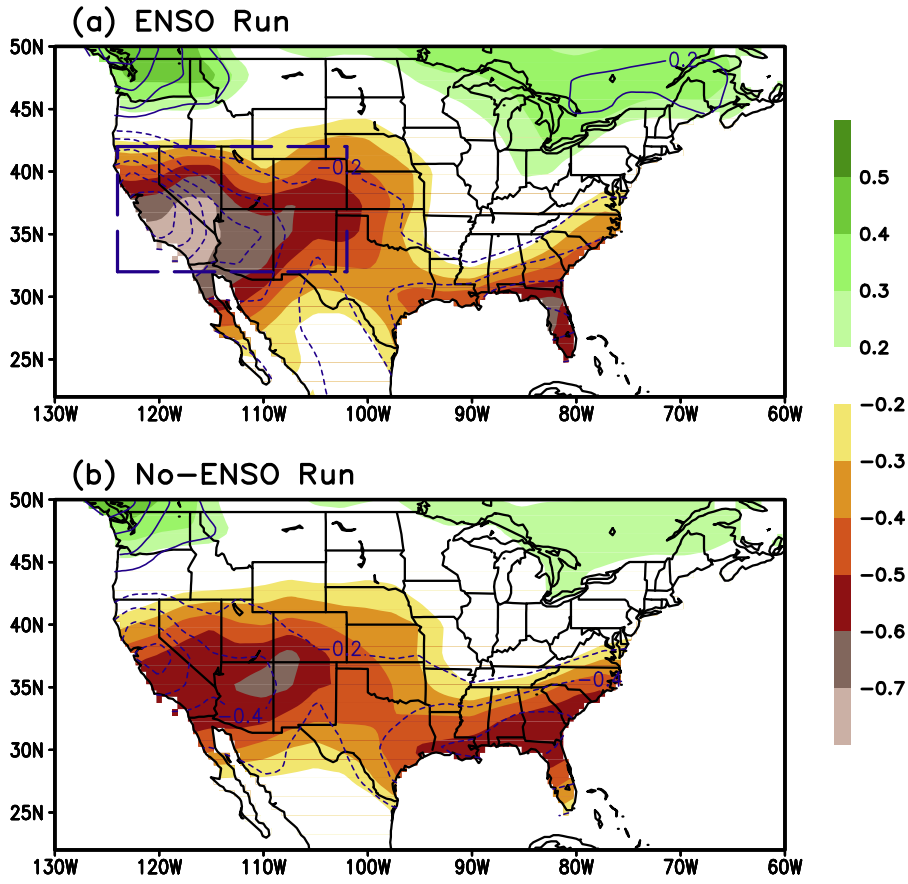


Fig. 3. Correlation (shadings) and regression coefficient (contours) of winter precipitation with the time series of the projection coefficients of precipitation anomalies onto the observed ENSO-related precipitation pattern (Fig. 2a) for (a) ENSO run and (b) no-ENSO run. The contour interval is same as in Fig. 2a. The box with blue long-dash lines in (a) denotes the southwestern region (32°N–42°N, 102°W–124°W) used in the following analysis. (For interpretation of the references to color in this figure legend, the reader is referred to the web version of this article.)

pattern are close to each other in the two runs. The largest difference with and without ENSO is the higher probability of the anomalous precipitation pattern with 3–4 year persistence in the ENSO run. These time bands are at the interannual timescale, coincident with the timescale of ENSO. In fact, the higher probability in the ENSO run is mainly due to a higher frequency of have three and four consecutive years of below normal precipitation in the

Southwest (not shown). In contrast, for the precipitation pattern persisting through 5–7 years, the occurrence is slightly higher in the no-ENSO run than in the ENSO run.

In addition to the PDF and CDF of total precipitation anomalies in the southwestern region (Fig. 5b and c), the PDF and CDF of precipitation anomalies in the same region reconstructed based on the linear regression against the time series of the projection coefficients are also shown in Fig. 5e and f. These are the precipitation anomalies at each grid point in the southwestern domain that are associated with the specific ENSO-like precipitation pattern (Fig. 3a and b). The differences in the PDF and CDF between the ENSO run and no-ENSO run display the same behavior as the total anomalies (Fig. 5b and c) for the annual, 3-, and 5-year means. The impact of ENSO on the characteristics of the southwestern precipitation is mainly through its effect on precipitation associated with the anomaly pattern in Fig. 3.

The comparison between the characteristics of Southwest winter precipitation in the ENSO run and no-ENSO run suggests that ENSO not only enhances the magnitude (or extremes) of precipitation anomalies, but also shifts precipitation variability toward lower frequencies. In the presence of ENSO, the chance for 3–4 year persistent precipitation anomalies, including prolonged drought in the U.S. Southwest, becomes higher. The physical processes involved are essentially a direct response of the atmosphere circulation to the tropical heating associated with ENSO and atmospheric teleconnections linking U.S. Southwest precipitation and tropical Pacific SST (e.g., Hoerling and Kumar, 2003; Wang and Schubert, 2014).

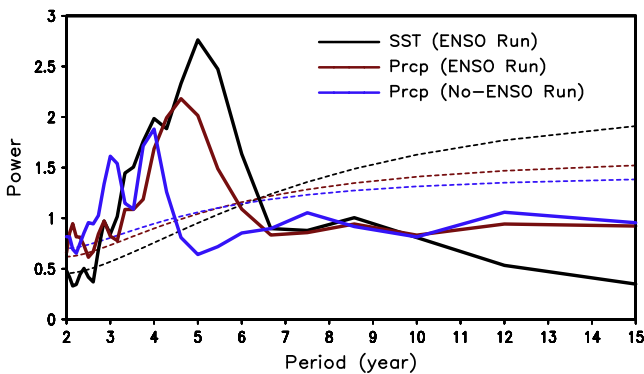


Fig. 4. Power spectra of the 480-year time series of the Niño 3.4 SST in the ENSO run (black), and the normalized projection coefficients for precipitation anomalies in the ENSO run (red) and no-ENSO run (blue). The power spectra are the averages over eight 60-year segments. Dashed lines are red-noise spectra. (For interpretation of the references to color in this figure legend, the reader is referred to the web version of this article.)

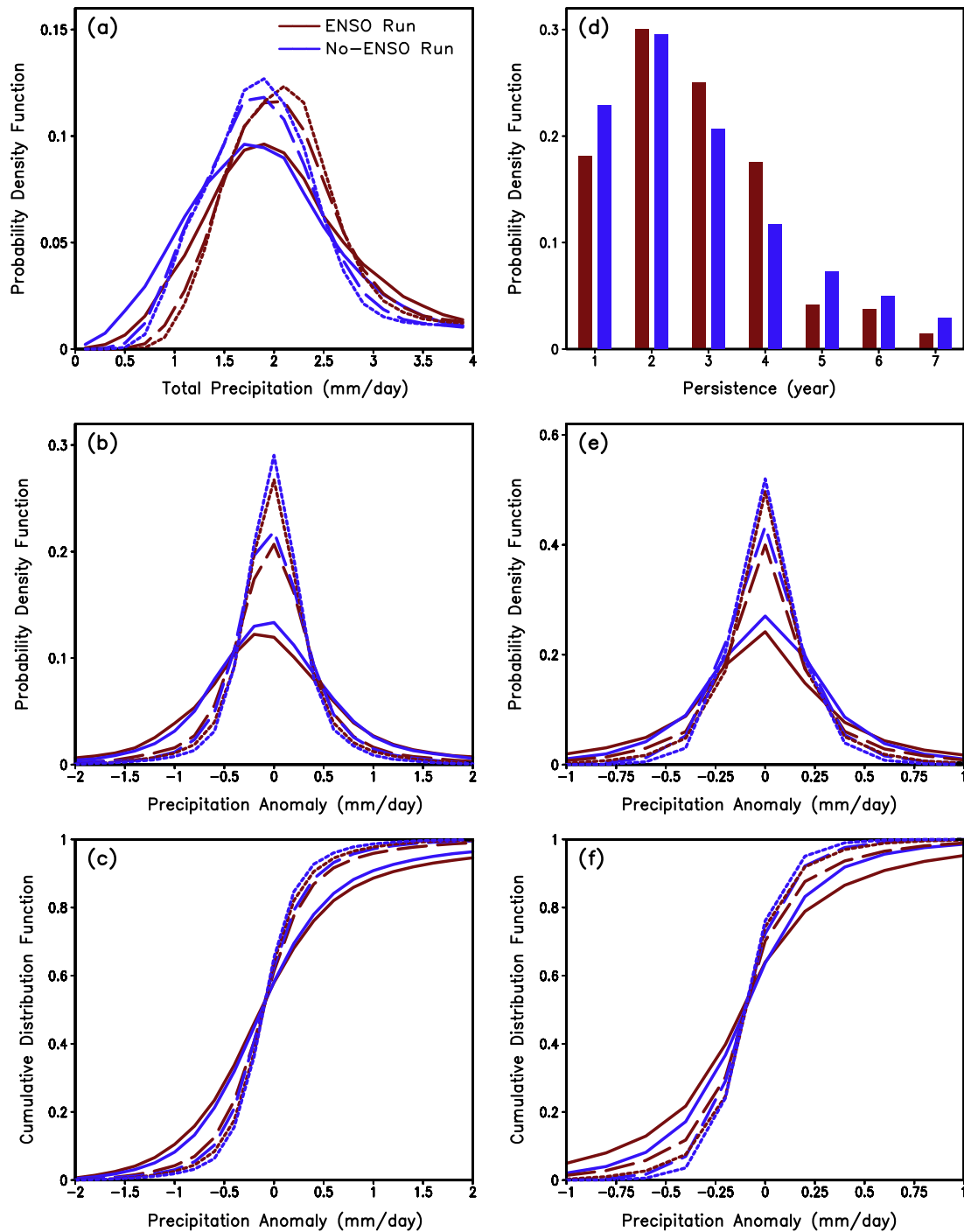


Fig. 5. Probability density function (PDF) of U.S. Southwest (a) JFM total precipitation, (b) precipitation anomaly, (d) persistence of the time series of the projection coefficients onto the SVD precipitation pattern, (e) reconstructed precipitation anomalies based on the time series of projection coefficients, and cumulative distribution function (CDF) of U.S. Southwest (c) JFM precipitation anomaly and (f) reconstructed precipitation anomalies based on the time series of projection coefficients. The unit for precipitation is mm day^{-1} . Red (blue) lines/bars are for the ENSO (no-ENSO) run. Solid, dash, and dot lines are for annual, 3-, and 5-year JFM mean precipitation, respectively. (For interpretation of the references to color in this figure legend, the reader is referred to the web version of this article.)

3.4. Atmospheric teleconnection linking ENSO and U.S. Southwest precipitation

The decadal changes in the co-variation between ENSO and Southwest precipitation over the three periods depicted by the first SVD mode (Fig. 2c) are further examined in terms of atmospheric teleconnection. Fig. 6 shows the correlation of observed 200-hPa height and linear regression of 200-hPa wind against the SVD1 precipitation time series (Fig. 2c) for the periods of 1948–1977,

1978–1999, and 2000–2014, respectively. The teleconnection in the upper atmosphere is characterized by a wave train across the Pacific/North American (PNA) region in all three periods. Associated with a drought in the U.S. Southwest (Fig. 2a), there are negative height anomalies and cyclonic circulation over the equatorial Pacific and Canada, and positive height anomalies and anticyclonic circulation over the North Pacific. The tropical circulation anomalies result from the atmospheric response to La Niña (Fig. 2b). An upper-level trough presents over the central North America, leading to dry

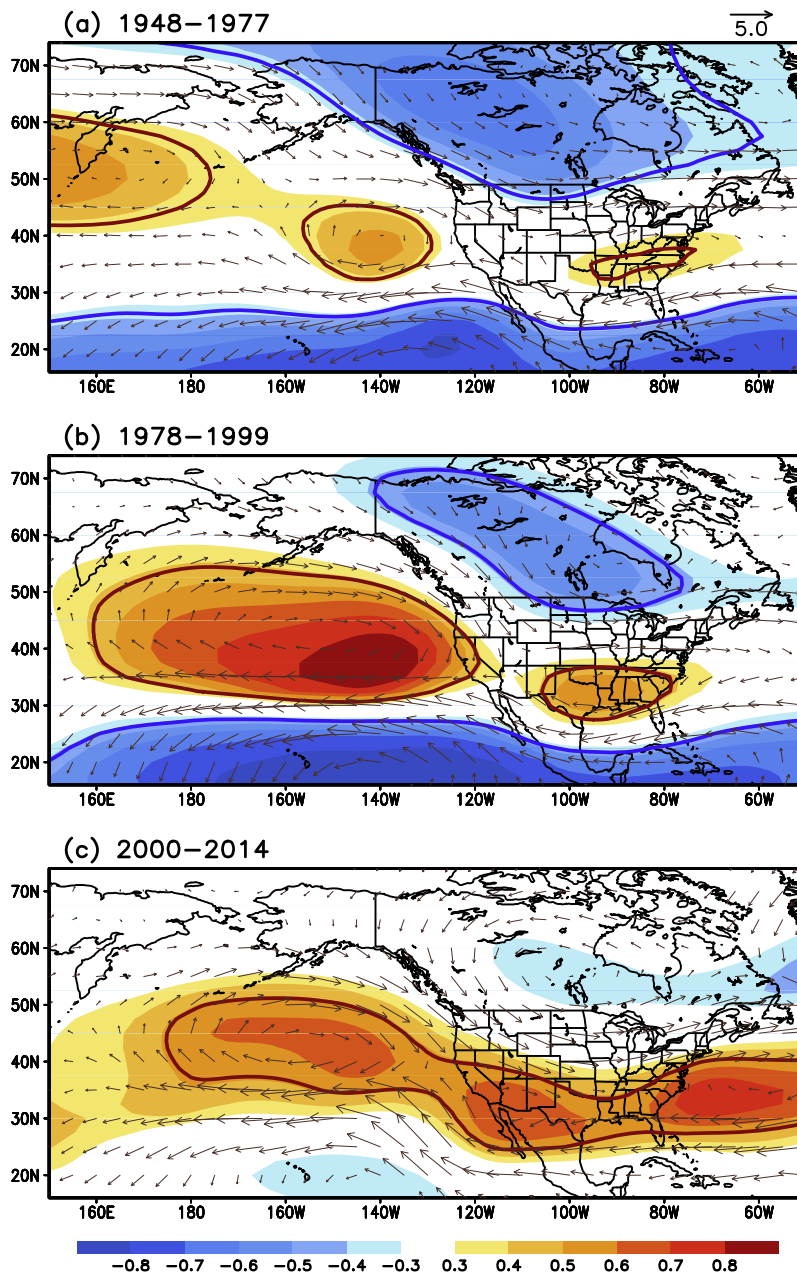


Fig. 6. Correlation (shadings) of JFM 200-hPa height and regression coefficient (vectors; m s^{-1}) of JFM 200-hPa wind vs. the SVD1 precipitation time series for the periods of (a) 1948–1977, (b) 1978–1999, and (c) 2000–2014, respectively. The areas circled by the thick red (blue) lines denote the positive (negative) correlations exceeding the 95% significance level after considering the degree of freedom of the data for each period. The regression anomalies are associated with a one-standard-deviation departure in the precipitation time series. (For interpretation of the references to color in this figure legend, the reader is referred to the web version of this article.)

conditions to the south of the upper-level jet entrance region, which is located in the U.S. Southwest (Fig. 2a). The trough also favors wet conditions in the jet exit region, as shown in Fig. 2a, from the Ohio River valley to the northeast of the Great Lakes.

Differences in the teleconnection among the three periods are also evident (Fig. 6). The correlation of 200-hPa height in the tropical Pacific with the SVD1 precipitation time series is strong in the first and second periods (Fig. 6a and b), but much weaker in the last period (Fig. 6c). This is consistent with the strength of the link between Southwest Precipitation and ENSO in different periods, as indicated by the high correlation (0.84) between the two SVD time series (Fig. 2c) in the two early periods and the low correlation (0.30) in the last 15 years. As the ENSO variability was relatively strong before 2000 and became weaker after that (Hu et al., 2013), the results in Fig. 6 may suggest that the strength of the link

between Southwest precipitation and the tropical circulation in response to ENSO over different epochs depends on the intensity of ENSO.

Additionally, as part of the teleconnection, the positive correlation with 200-hPa height over the North Pacific in Fig. 6a is much weaker than that in Fig. 6b. Since La Niña (El Niño) occurred more frequently in the first (second) period (Fig. 2c), the difference between Fig. 6a and b may imply an asymmetry in the extratropical circulation response to ENSO between warm and cold phases. Specifically, the circulation response to El Niño over the North Pacific may be stronger than the response to La Niña, the nonlinearity of ENSO response (Hoerling et al., 1997, 2001).

Both the common and uncommon circulation features in the three periods can also be seen in the lower atmosphere. Fig. 7 shows the regression coefficients of SLP and 850-hPa wind against

the SVD1 precipitation time series (Fig. 2c) for the three periods, respectively. Associated with the anticyclonic circulation over the North Pacific, offshore flows prevail along the California coast in all the three periods, which cause a deficit of moisture flux from the North Pacific Ocean to the U.S. Southwest. There are negative SLP anomalies that occur in the central tropical Pacific in the two early periods (Fig. 7a and b), but not in the third period (Fig. 7c). Similar to the upper level, the lower-level circulation anomalies over the North Pacific in the first period are also much weaker than those in the second period.

It has been noted (e.g., Kistler and Kalnay, 2000) that discontinuities in tropospheric signals exist over the Pacific prior to the 1960s in the NCEP–NCAR Reanalysis. The intraseasonal variability in the western Pacific is also considerably weaker in the early years of the reanalysis data. These biases might affect the results presented in Figs. 6 and 7.

The number of ENSO events in the observations is very limited during each of the three periods. The sensitivity of the drought-related circulation response to different phase and intensity of ENSO, however, can be assessed with the 480-year ENSO run, which has sufficient number of ENSO events for performing a statistically meaningful analysis. Similar to Trenberth (1997) using the Niño 3.4 SST index to define ENSO events, we define an El Niño (La Niña) when the JFM seasonal mean Niño 3.4 SST index is greater than 0.5 K (less than -0.5 K). Additionally, we categorize an ENSO event as a strong (weak) event if the magnitude of the Niño 3.4 index is greater than 1 K (between 0.5 K and 1 K). With these criteria, a total of 140 El Niño and 148 La Niña events are identified in the 480-year ENSO run. Among them, 66 and 74 (57 and 91) events are strong and weak El Niño (La Niña), respectively.

Fig. 8 shows the correlation of JFM 200-hPa height with the time series of projection coefficients of JFM model precipitation

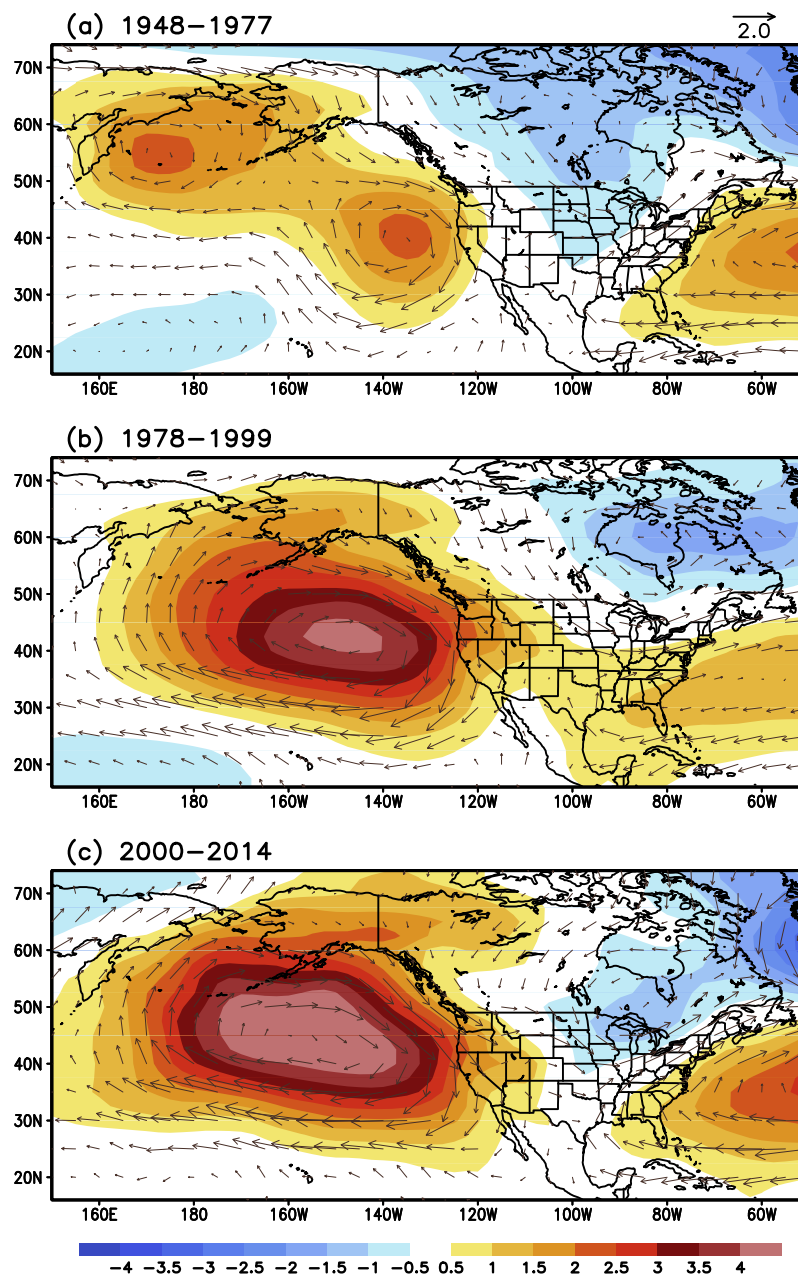


Fig. 7. Regression coefficients of JFM SLP (shadings; hPa) and 850-hPa wind (vectors; m s^{-1}) vs. the SVD1 precipitation time series for the periods of (a) 1948–1977, (b) 1978–1999, and (c) 2000–2014, respectively. The regression anomalies are associated with a one-standard-deviation departure in the precipitation time series.

onto the SVD1 precipitation pattern (Fig. 2a) over the years of different ENSO categories. The correlation between the precipitation over the Southwest and the 200-hPa height over the North Pacific is stronger during El Niño (Fig. 8a) than during La Niña (Fig. 8b), consistent with those seen in the observations (Fig. 6a and b). The asymmetry between the cold and warm phases is more obvious for strong ENSO events (Fig. 8c and d). Compared to the observations (Fig. 6a and b), regions of positive correlations in the model extend more eastward across the Southwest. This is a CFS model bias in the circulation response to ENSO.

Fig. 8 also illustrates the sensitivity of the teleconnection to the intensity of ENSO. The correlation over the PNA region is much larger in strong El Niño years (Fig. 8c) than in weak El Niño years (Fig. 8e). In contrast, the teleconnection is less sensitive to the intensity of La Niña (Fig. 8d and f). This is due to the nonlinearity of tropical deep convection driven by SST. For warm SSTs higher than 28 °C, a threshold for atmospheric deep convection (Fu et al., 1994), the intensity of deep convection is very sensitive to the changes in SST because saturation vapor pressure is an exponential function of SST. On the other hand, when SSTs are colder than 28 °C, no deep convection occurs. Consequently, the associated anomalous tropical heating is insensitive to the changes in SST.

The sensitivity of the teleconnection to the phase and intensity of ENSO may explain the decadal changes in the strength of the link between Southwest precipitation and ENSO. The weaker circulation response to ENSO over the North Pacific in the first period (1948–1977) than in the second period (1978–1999) is due to the asymmetry of the circulation response to different phases of

ENSO between the two periods (Trenberth and Stepaniak, 2001; Wang, 1995). The link between Southwest precipitation and ENSO is weakest in the third period (2000–2014), resulting from the weakening of the ENSO variability since 2000 (Hu et al., 2013).

The Southwest drought-related circulation anomalies in the ENSO run are compared with those in the no-ENSO run. Fig. 9a–d present the correlation coefficient for 200-hPa height and linear regression coefficients for 200-hPa and 850-hPa winds and SLP with the 480-year time series of projection coefficients of model precipitation onto the SVD1 precipitation pattern (Fig. 2a) for the ENSO run and no-ENSO run, respectively. Associated with a Southwest drought, local upper-level and lower-level circulation anomalies in the ENSO run (Fig. 9a and b) are similar to those in the no-ENSO run (Fig. 9c and d), including upper-level anticyclonic circulation and positive SLP anomalies over the Southwest, and off-shore flows along the California coast. However, the large-scale circulation anomalies over the PNA region are different between the two simulations. Their spatial scale is larger in the ENSO run than in the no-ENSO run, consistent with the temporal scale of precipitation shifting toward lower frequencies in the ENSO run (Fig. 4). The circulation anomalies are stronger in the ENSO run than in the no-ENSO run, which is another indicator of the ENSO impact on the drought-related circulation, leading to larger precipitation anomalies over the Southwest in the ENSO run (Fig. 3).

The drought-related circulation patterns in the two simulations are also compared with those associated with the current Southwest drought. The persistence of the Southwest drought from 2011 to the present (2014) can be seen in the time series of the first SVD mode

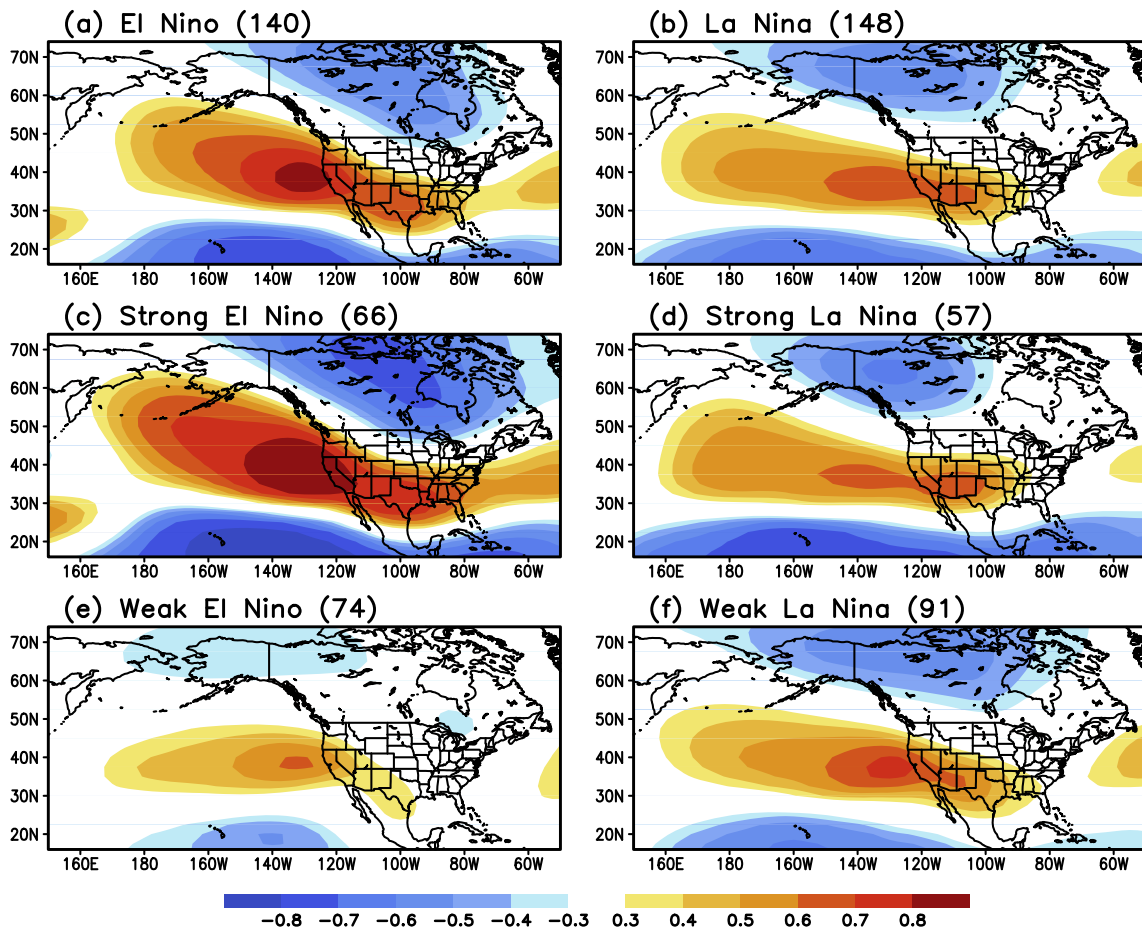


Fig. 8. Correlation of JFM 200-hPa height with the time series of projection coefficients of JFM model precipitation onto the SVD1 precipitation pattern (Fig. 2a) for (a) all El Niño, (b) all La Niña, (c) strong El Niño, (d) strong La Niña, (e) weak El Niño, and (f) weak La Niña years in the 480-year ENSO run. All correlation coefficients exceeding 0.3 are above the 95% significance level. The integer in parentheses at the top of each panel is the number of events for each ENSO category defined by the Niño 3.4 SST index.

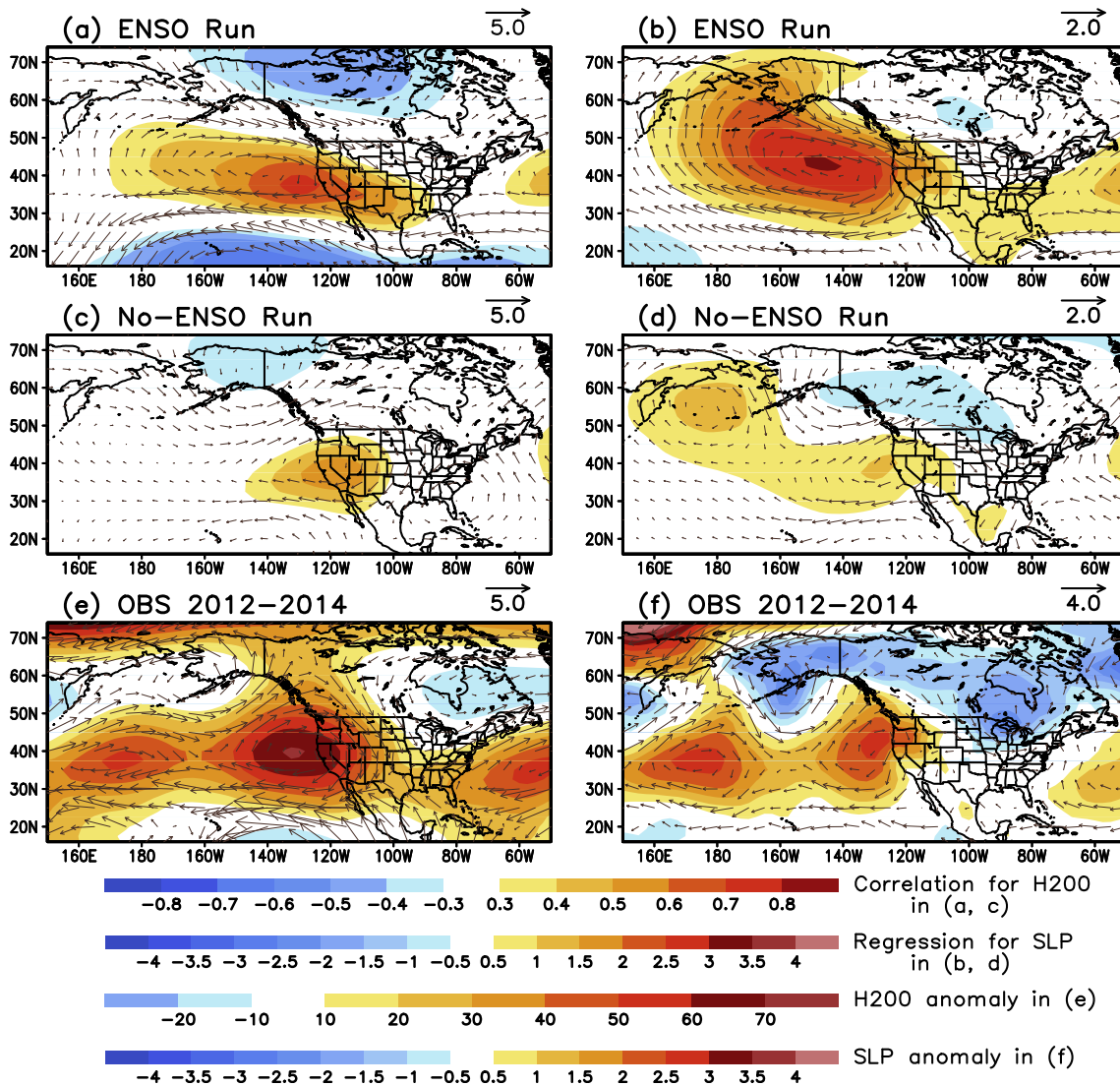


Fig. 9. Correlation (shadings) of JFM 200-hPa height and regression coefficient (vectors; m s^{-1}) of JFM 200-hPa wind vs. the 480-year time series of projection coefficients of JFM model precipitation onto the SVD1 precipitation pattern (Fig. 2a) for (a) ENSO run and (c) no-ENSO run, similar regression coefficients of JFM SLP (shadings; hPa) and 850-hPa wind (vectors; m s^{-1}) for (b) ENSO run and (d) no-ENSO run, and 3-year (2012–2014) mean anomalies of (e) JFM 200-hPa height (shadings; gpm) and wind (vectors; m s^{-1}) and (f) SLP (shadings; hPa) and 850-hPa wind (vectors; m s^{-1}). The regression anomalies in (a)–(d) are associated with a one-standard-deviation departure in the time series of precipitation projection coefficients.

(Fig. 2c) with positive coefficients for precipitation (Fig. 2a) in the last four years. Except for the La Niña in 2011, the coefficients for the SST field (Fig. 2b) are small from 2012 to 2014, indicating an ENSO neutral condition. Fig. 9e and f show the upper-level and lower-level circulation anomalies averaged over the JFM of 2012–2014 when a severe drought occurred in the U.S. Southwest, but without La Niña in the tropical Pacific. The local circulation exhibits similarity to both the ENSO run and no-ENSO run, including the anticyclonic circulation over the Southwest with positive height and SLP anomalies, and offshore flows along the California coast. In the absence of La Niña, there is no well-defined wave train originating from the tropical Pacific at the upper level (Fig. 9e). At the lower level (Fig. 9f) the circulation over the PNA region bears more resemblance to the no-ENSO run (Fig. 9d) than to the ENSO run (Fig. 9b), with relatively small spatial scales over the North Pacific.

4. Conclusions

The impact of ENSO on U.S. Southwest precipitation and drought has been examined in this study using both observations

and CFS coupled model simulations with and without ENSO. The SVD analysis was applied to the 67-year winter U.S. precipitation and Pacific SST. The leading SVD mode represents the coupled variability between ENSO and Southwest precipitation. Results indicate strong associations between Southwest drought and La Niña during 1948–1977 and between Southwest pluvial and El Niño during 1978–1999. The relationship between Southwest precipitation and the ENSO SST in the tropical eastern and central Pacific tended to be weaker since 2000.

A comparison between the 480-year ENSO run and no-ENSO suggests that ENSO can alter the characteristics of precipitation, thus drought over the Southwest in terms of frequency and intensity. ENSO shifts Southwest precipitation toward lower frequencies. In the presence of ENSO, precipitation anomalies tend to have larger extremes and the variability of precipitation is thus enhanced. In addition, the chance for the ENSO-like precipitation pattern to persist over 3–4 years is higher in the ENSO run than in the no-ENSO run.

The sensitivity of the Southwest precipitation-related teleconnection to both the phase and intensity of ENSO was also assessed

with the ENSO run. It was demonstrated that the link between Southwest precipitation and the circulation over the North Pacific is stronger during El Niño than during La Niña. The circulation response to ENSO is more sensitive to the change in El Niño SST and less sensitive to the change in La Niña SST. Given the decadal changes in the occurrence frequency and the variability of El Niño and La Niña over the 67 years, the sensitivity and asymmetry of the circulation response to ENSO help in understanding the observed decadal changes in the strength of the relationship between Southwest precipitation and large-scale circulation anomalies over the PNA region.

Acknowledgments

This work was supported by the NOAA Climate Program Office's Modeling, Analysis, Predictions, and Projections program. We thank two anonymous reviewers and the editor for their insightful and constructive comments and suggestions.

References

- Andrade, E.R., Sellers, W.D., 1988. El Niño and its effect on precipitation in Arizona. *J. Climatol.* 8, 403–410.
- Bretherton, C.S., Smith, C., Wallace, J.M., 1992. An intercomparison of methods for finding coupled patterns in climate data. *J. Clim.* 5, 541–560.
- Cayan, D.R., Dettinger, M.D., Diaz, H.F., Graham, N.E., 1998. Decadal variability of precipitation over western North America. *J. Clim.* 11, 3148–3166.
- Cayan, D.R., Redmond, K.T., Riddle, L.G., 1999. ENSO and hydrologic extremes in the western United States. *J. Clim.* 12, 2881–2893.
- Chen, M., Xie, P., Janowiak, J.E., Arkin, P.A., 2002. Global land precipitation: A 50-yr monthly analysis based on gauge observations. *J. Hydrometeorol.* 3, 249–266.
- Cook, B.I., Cook, E.R., Anchukaitis, K.J., Seager, R., Miller, R.L., 2011. Forced and unforced variability of twentieth century North American droughts and pluvials. *Clim. Dynam.* 37, 1097–1110.
- Dettinger, M.D., Cayan, D.R., Diaz, H.F., Meko, D.M., 1998. North-south precipitation patterns in western North America on interannual-to-decadal timescales. *J. Clim.* 11, 3095–3111.
- Fu, R., Del Genio, A.D., Rossow, W.B., 1994. Influence of ocean surface conditions on atmospheric vertical thermodynamic structure and deep convection. *J. Clim.* 7, 1092–1108.
- Funk, C., Hoell, A., Stone, D., 2014. Examining the contribution of the observed global warming trend to the California droughts of 2012/13 and 2013/14. (In Explaining Extreme Events of 2013 from a Climate Perspective). *Bull. Amer. Meteor. Soc.* 95, S11–S15.
- Hoerling, M.P., Kumar, A., 2003. The perfect ocean for drought. *Science* 299, 691–699.
- Hoerling, M.P., Kumar, A., Zhong, M., 1997. El Niño, La Niña, and the nonlinearity of their teleconnections. *J. Clim.* 10, 1769–1786.
- Hoerling, M.P., Kumar, A., Xu, T., 2001. Robustness of the nonlinear climate response to ENSO's extreme phases. *J. Clim.* 14, 1277–1293.
- Hu, Z.-Z., Kumar, A., Ren, H.-L., Wang, H., L'Heureux, M., Jin, F.-F., 2013. Weakened interannual variability in the tropical Pacific Ocean since 2000. *J. Clim.* 26, 2601–2613.
- Jia, L. et al., 2015. Improved seasonal prediction of temperature and precipitation over land in a high-resolution GFDL climate model. *J. Clim.* <http://dx.doi.org/10.1175/JCLI-D-14-00112.1>, in press.
- Kalnay, E. et al., 1996. The NCEP–NCAR 40-Year Reanalysis Project. *Bull. Amer. Meteor. Soc.* 77, 437–471.
- Kim, S.T., Yu, J.-Y., Kumar, A., Wang, H., 2012. Examination of the two types of ENSO in the NCEP CFS model and its extratropical associations. *Mon. Wea. Rev.* 140, 1908–1923.
- Kistler, R., Kalnay, E., 2000. The NCEP/NCAR reanalysis prior to 1958. In: *Proc. Second WRC Int. Conf. on Reanalyses*, Wokefield Park, United Kingdom, WMO, pp. 27–35.
- Kumar, A., Wang, H., Wang, W., Xue, Y., Hu, Z.-Z., 2013. Does knowing the oceanic PDO phase help predict the atmospheric anomalies in subsequent months? *J. Clim.* 26, 1268–1285.
- Mantua, N.J., Hare, S.R., Zhang, Y., Wallace, J.M., Francis, R., 1997. A Pacific interdecadal climate oscillation with impacts on salmon production. *Bull. Amer. Meteor. Soc.* 78, 1069–1079.
- McCabe, G.J., Dettinger, M.D., 1999. Decadal variations in the strength of ENSO teleconnections with precipitation in the western United States. *Int. J. Climatol.* 19, 1399–1410.
- McCabe, G.J., Palecki, M.A., Betancourt, J.L., 2004. Pacific and Atlantic Ocean influences on multidecadal drought frequency in the United States. *Proc. Natl. Acad. Sci. USA* 101, 4136–4141.
- Mo, K.C., Schemm, J.-K.E., Yoo, S.-H., 2009. Influence of ENSO and the Atlantic multidecadal oscillation on drought over the United States. *J. Clim.* 22, 5962–5982.
- Moorthi, S., Pan, H.-L., Caplan, P., 2001. Changes to the 2001 NCEP operational MRF/AVN global analysis/forecast system. *NWS Tech. Procedures Bull.* 484, pp. 14 <<http://www.nws.noaa.gov/om/tpb/484.htm>>.
- Ogata, T., Xie, S.-P., Wittenberg, A., Sun, D.-Z., 2013. Interdecadal amplitude modulation of El Niño–Southern Oscillation and its impact on tropical Pacific decadal variability. *J. Clim.* 26, 7280–7297.
- Pacanowski, R.C., Griffies, S.M., 1998. MOM 3.0 Manual. NOAA/Geophysical Fluid Dynamics Laboratory, pp. 668.
- Pan, H.-L., Mahrt, L., 1987. Interaction between soil hydrology and boundary layer developments. *Bound.-Layer Meteorol.* 38, 185–202.
- Pejgon, P.J., Kumar, A., 2010. Multimodel estimates of atmospheric response to modes of SST variability and implications for droughts. *J. Clim.* 23, 4327–4341.
- Reynolds, R.W., Rayner, N.A., Smith, T.M., Stokes, D.C., Wang, W., 2002. An improved in situ and satellite SST analysis for climate. *J. Clim.* 15, 1609–1625.
- Ropelewski, C.F., Halpert, M.S., 1986. North American precipitation and temperature patterns associated with the El Niño/Southern Oscillation (ENSO). *Mon. Wea. Rev.* 114, 2352–2362.
- Saha, S. et al., 2006. The NCEP climate forecast system. *J. Clim.* 19, 3483–3517.
- Schubert, S. et al., 2009. A U.S. CLIVAR project to assess and compare the response of global climate models to drought-related SST forcing patterns: overview and results. *J. Clim.* 22, 5251–5272.
- Seager, R., Hoerling, M., 2014. Atmosphere and ocean origins of North American droughts. *J. Clim.* 27, 4581–4606.
- Seager, R., Burgman, R., Kushnir, Y., Clement, A., Cook, E., Naik, N., Miller, J., 2008. Tropical Pacific forcing of North American medieval megadroughts: testing the concept with an atmospheric model forced by coral-reconstructed SSTs. *J. Clim.* 21, 6175–6190.
- Smith, T.M., Reynolds, R.W., Peterson, T.C., Lawrimore, J., 2008. Improvements to NOAA's historical merged land–ocean surface temperature analysis (1880–2006). *J. Clim.* 21, 2283–2296.
- Swain, D.L., Tsiang, M., Haugen, M., Singh, D., Charland, A., Rajaratnam, B., Diffenbaugh, N.S., 2014. The extraordinary California drought of 2013/2014: character, context, and the role of climate change. (In Explaining Extreme Events of 2013 from a Climate Perspective). *Bull. Amer. Meteor. Soc.* 95, S3–S7.
- Tang, Y., Deng, Z., Zhou, X., Cheng, Y., Chen, D., 2008. Interdecadal variation of ENSO predictability in multiple models. *J. Clim.* 21, 4811–4833.
- Ting, M., Wang, H., 1997. Summertime United States precipitation variability and its relation to Pacific sea surface temperature. *J. Clim.* 10, 1853–1873.
- Trenberth, K.E., 1997. The definition of El Niño. *Bull. Amer. Meteor. Soc.* 78, 2771–2777.
- Trenberth, K.E., Hoar, T.J., 1996. The 1990–1995 El Niño–Southern Oscillation event: longest on record. *Geophys. Res. Lett.* 23, 57–60.
- Trenberth, K.E., Stepaniak, D.P., 2001. Indices of El Niño evolution. *J. Clim.* 14, 1697–1701.
- Wallace, J.M., Smith, C., Bretherton, C.S., 1992. Singular value decomposition of wintertime sea surface temperature and 500-mb height anomalies. *J. Clim.* 5, 561–576.
- Wang, B., 1995. Interdecadal changes in El Niño onset in the last four decades. *J. Clim.* 8, 267–285.
- Wang, H., Fu, R., 2000. Winter monthly mean atmospheric anomalies over the North Pacific and North America associated with El Niño SSTs. *J. Clim.* 13, 3435–3447.
- Wang, H.-L., Schubert, S., 2014. The precipitation response over the continental United States to cold tropical Pacific sea surface temperatures. *J. Clim.* 27, 5036–5055.
- Wang, H., Ting, M., 2000. Covariabilities of winter U.S. precipitation and Pacific sea surface temperature. *J. Clim.* 13, 3711–3719.
- Wang, H., Kumar, A., Wang, W., Xue, Y., 2012a. Seasonality of the Pacific decadal oscillation. *J. Clim.* 25, 25–38.
- Wang, H., Kumar, A., Wang, W., Xue, Y., 2012b. Influence of ENSO on Pacific decadal variability: an analysis based on the NCEP climate forecast system. *J. Clim.* 25, 6136–6151.
- Wang, S.-Y., Hipps, L., Gillies, R.R., Yoon, J.-H., 2014. Probable causes of the abnormal ridge accompanying the 2013–2014 California drought: ENSO precursor and anthropogenic warming footprint. *Geophys. Res. Lett.* 41, 3220–3226.